LAWRENCE
LIVERMORE
NATIONAL
LABORATORY

LLNL-JRNL-865276

Electrostatic Dissipation in 3D-Printable Silicone

J. A. Armas, M. J. Ford, K. P. Foster, T. Hall, C. K. Loeb, K. L. Baron, L. X. Perezperez, F. Xie, T. Bryson, S. Schmidt, J. M. Lenhardt

June 5, 2024

American Chemical Society Applied Materials and Interfaces

Disclaimer

Electrostatic dissipation in 3D-printable silicone

Jeremy A. Armas, Michael J. Ford, Kenton P. Foster, Terence Hall, Colin K. Loeb, Spencer Schmidt, Stanley F. Williams, Kathlyn L. Baron, Lemuel X. Pérez Pérez, Fangyou Xie, Taylor M. Bryson, Jeremy M. Lenhardt*

Lawrence Livermore National Laboratory, Livermore, California 94550, United States

*****Email: armas3@llnl.gov

KEYWORDS: 3D printing, silicone, polysiloxane, electrostatic dissipative, carbon nanotubes

ABSTRACT: In this report, we describe the incorporation of single walled carbon nanotubes (CNTs) into 3D printable siloxane elastomers for electrostatic dissipation. The composite was characterized, focusing on how rheological and mechanical properties of the siloxane are affected at various CNT loading levels. Electrical properties were also characterized to develop materials with effective electrostatic dissipation. We demonstrate that low loadings (<1 wt. %) of CNT can be sufficiently dispersed into silicone resins that can be 3D printed, and the resulting material shows a significant improvement in electrostatic dissipation through the reduction in electrical resistivity with minimal effect on its mechanical properties.

1. INTRODUCTION:

3D printing is a rapidly growing manufacturing method that has been utilized to develop components for a variety of applications such as three-dimensional antennas,[1] carbon capture

reactors,[2] supercapacitors,[3,4] stimuli responsive materials,[5,6] syntactic foams,[7] shape memory materials,[8] hydrogen capturing materials,[9] and carbon-fiber reinforced composites[10]. 3D printing also enables the production of cellular foams with customizable pore architecture to achieve compressive mechanical properties that can be tailored to minimize permanent deformation by evenly distributing stress throughout the printed architecture.[11,12] In addition to precise control of print architecture, 3D printing is amenable to custom resins that can be tuned to precisely control the material's intrinsic properties.[13]

Within the breadth of 3D printing techniques, direct ink writing (DIW) is an extrusion process wherein a paste with controlled rheological properties is deposited in a layer-by-layer manner to build up 3-dimensional structures. This manufacturing process serves as a versatile alternative to conventional manufacturing, offering the capability to customize material formulations to address specific application requirements.[14] DIW can be used to print many classes of materials including silicone resins, which are of interest due to their low volatility, good elasticity, and broad thermal stability among other properties. In these silicone resins, the addition of additives such as hydrophobically-modified silica fillers along with silicone polyether copolymers have been demonstrated to impart good print resolution of the deposited print strand, which enables architectures with tailored porosity.[13,15,16] Silicones that are processed using DIW have been applied in areas like wearable technology[17–19], soft robotics[14,15], and structural components.[18]

Early reports demonstrated the DIW printing of silicone structures with tunable mechanical properties using commercial resins.[11,21,22] As research on 3D printable silicones has expanded, new formulations have expanded the formulation space to control resin thixotropy and material properties.[13,19,23] Recent progress in this field has focused on developing new resin systems with

bespoke functionality, such as for shape memory[8], dielectric elastomers[24], and stimuli responsive materials.[25]

To develop new functional resins, additives that have useful intrinsic properties can be added to impart functionality into the resulting composite materials. One such filler class of interest is conductive fillers, which can be mixed into silicone resins to reduce. Previous reports have demonstrated the use of DIW to create conductive silicone structures with reduced resistance by incorporating conductive fillers into the resins.[18,26–31] As the conductive filler loading in the resin system is increased, fillers form percolative networks at a volume fraction loading defined as the percolation threshold, $\Phi_c \propto 1/\eta$, where η is the particle aspect ratio for random distributions of filler.[32] Single walled carbon nanotubes (CNTs) are a good candidate for conductive additives since they typically have large aspect ratios, resulting in statistical percolation thresholds usually below 1 wt. %, whereas the percolation threshold of low aspect ratio fillers such as carbon black ranges from 3 to 15 wt. % (**Figure 1a**).[33,34] CNT composites offer the added benefit of reduced environmental contamination compared to conventional carbon black composites, which often suffer from issues with sloughing, or the shedding of carbon black particles from the polymer matrix.[35,36]

Typically, printable conductive silicones are loaded to the point where the volume fraction of conductive particles was much greater than *Φc*, resulting in highly conductive composites that are suitable for use in soft circuitry and sensing.[37] However, for certain applications such as packaging for electrostatic discharge (ESD) protection, these conductive silicones may not be suitable. While conductive materials have surface resistivities below 10^5 Ω/sq, ESD-safe materials are generally defined to have surface resistivities between 10^5 Ω/sq and 10^9 Ω/sq. In these ranges,

the ESD-safe materials behave as a soft ground and neutralize charges at a slow, controlled rate to prevent excessive charge decay and thermal damage to circuitry.[38]

ESD is a significant concern in the chemical and electronics industries, leading to substantial equipment and component failure, which can lead to increased costs and possible workplace injury.[39–41] In electronics, ESD often causes integrated circuit (IC) failures due to rapid voltage and current discharges from charged objects like human fingers or tools. These discharges typically occur during production and assembly due to inadequate ESD control but can also happen during the IC's operational life. The miniaturization of ICs has made circuitry more susceptible to ESD damage, with common ICs like complementary metal-oxide semiconductor (CMOS) chips being damaged by voltages under 1 kV and newer microprocessors like very large-scale integration (VLSI) chips being damaged by voltages under 500 V.[42–45] Human body ESD can exceed several kilovolts, posing a significant risk to these sensitive ICs if unprotected. The goal of ESD safety is to equalize electrical potential. ESD shielding materials help control electrostatic charge accumulation, essential during fabrication, transportation, and operational use to prevent IC failures.[46,47] Elastomeric ESD shielding materials also protect ICs from mechanical shock and vibration, ensuring comprehensive device safety.

Previous reports have demonstrated the use of 3D printing to create ESD-safe polymer composites utilizing techniques such as stereolithography (SLA) and fused deposition modeling (FDM).[48–50] These reports generally focus on the use of commercial and custom thermoplastics that have limited compliance or strain at break. Herein, we report on the printing of elastomeric silicone foams that can be used as packaging for mechanical and electrical protection for electronics by optimizing static dissipative properties. We describe a method for incorporating CNTs, using a concentrate that contains CNTs and silicone polymer, into our resin systems.

In the process of developing these formulations, we considered the effects of CNTs and rheological additives on the rheological and mechanical properties (**Figure 1b**). The formulations developed for ESD take advantage of the combination of hexamethyldisilazane (HMDZ)-treated fumed silica, with a silicone polyether thixotropic modifier to improve the ink's print structure.[51,52] This approach differs from previous approaches, which typically use conductive fillers as rheological modifiers in unreinforced resins to increase the storage modulus and yield stress of their ink for printability.[30,53] The need for a minimal loading of functional filler to create a suitable resin for printing is eliminated by removing the dependence on the conductive filler as a rheological additive. The addition of these rheological modifiers also allows for the printing of gap-spanning structures with small nozzle sizes, which results in the ability to print tailored porosity in three dimensions at high resolutions. The addition of HMDZ-treated silica filler also serves as a mechanical reinforcing agent, which has been demonstrated to improve the tensile strength of elastomeric materials.[13,54,55]

The resulting mechanical and electrical properties manifest from the hierarchical structure of the printed architecture and the CNT morphology (**Figure 1c**). We characterized these resulting formulations to demonstrate printability to create porous architectures, robust mechanical behavior, and significant charge dissipation properties suitable for ESD protection, where electrical discharge can be dissipated through the printed composite (**Figure 1d, Video S1**). We then directly printed an ESD-safe protective foam onto a circuit board using structured light scanning to generate a custom print toolpath (**Figure 1e**). This demonstration shows that this technology can be used to print custom ESD-safe soft packaging directly onto complex substrate surfaces for electrical and mechanical protection for sensitive circuitry and can be used with

previously developed 3D printed electronic systems to produce robust, integrated printed circuitry for applications in fields like robotics, aerospace, and healthcare.

2. RESULTS & DISCUSSION:

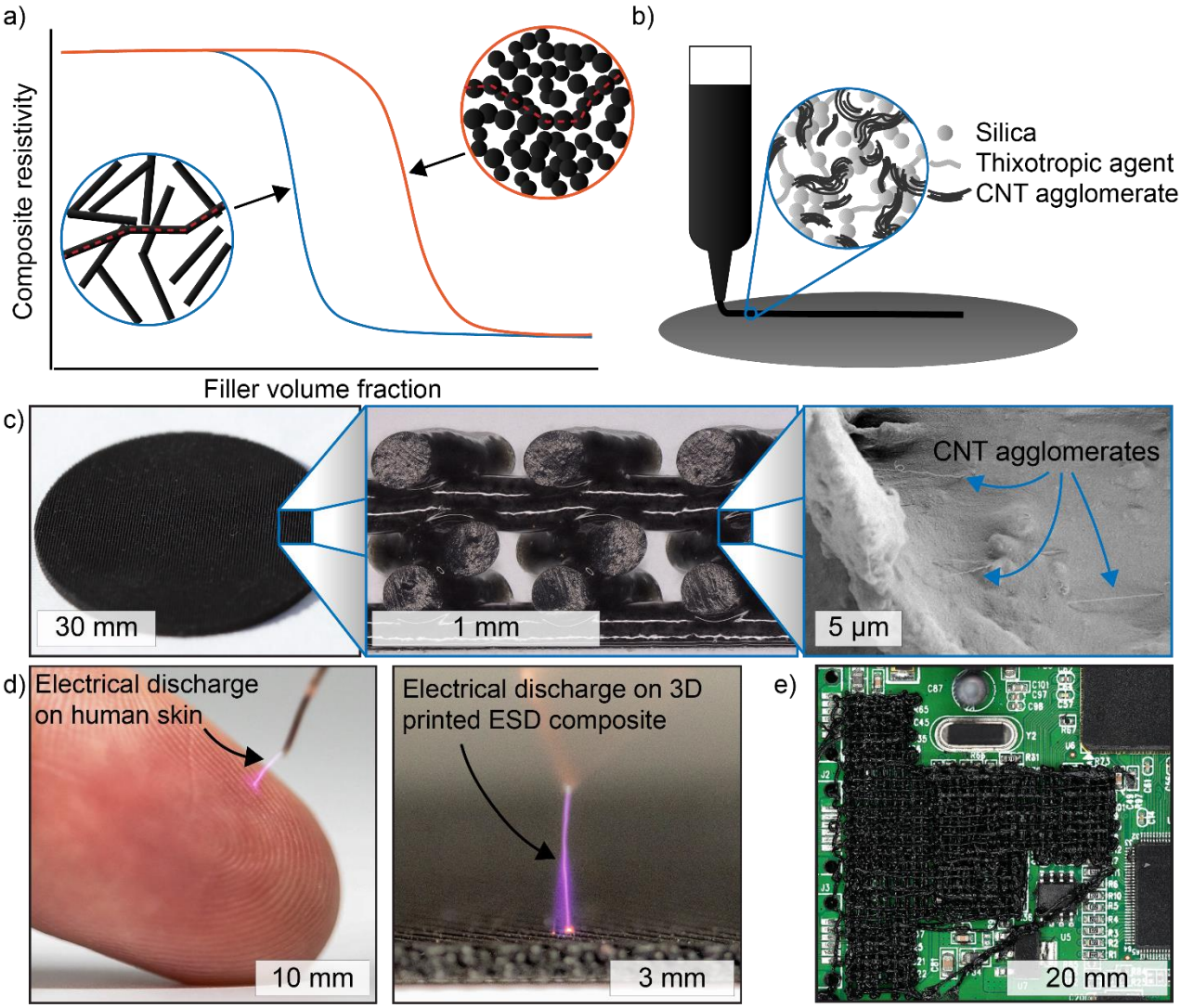

Figure 1. Overview of 3D-printable silicone composite for ESD. (a) Representation of random packing of high aspect-ratio conductive fillers, which results in a lower loading to form resistive pathways compared to isotropic fillers. (b) A thixotropic resin for electrostatic dissipative materials includes functional additives like silica for reinforcement, CNT to impart dissipative resistive pathways for charge transfer, and thixotropic agent to control the rheological behavior for DIW printing. (c) Overview image of an ESD-safe silicone structure showing a printed structure; a cross section of CNT loaded silicone where strands are oriented in a helicoidal pattern offset by 60°; and a micrograph of an ESD silicone cross section, with CNT agglomerates denoted with arrows. (d) Electrostatic discharge visibly observed on human skin and onto a 3D printed ESD foam. (e) Example of an ESD silicone directly printed onto a circuit board using DIW.

2.1 Incorporation of CNTs

In practice, filler mix quality and degree of agglomeration can greatly affect electrical performance of the final composite, so an optimized mixing process is required to develop a

composite with good electrical properties.[33,56] A mixing study was performed to determine efficient mixing parameters for incorporating 5.5 wt. % of a CNT concentrate into the silicone base. These resins were mixed by planetary mixing (**Figure 2a**) and cast onto glass slides using a 10 µm drawdown bar to inspect the quality of incorporation of the CNTs. After the first mix, large agglomerates of unincorporated CNT concentrate can be visually seen in the film and in 100× micrographs, and smaller scale aggregates of CNT can be seen in 1000× micrographs (**Figure 1b**). Large clumps of CNT concentrate are observed throughout the sample until after the third mix cycle, and in subsequent mixes agglomerates appear to become smaller. After the fourth mix, no noticeable agglomerates can be observed. By the fifth mix, the CNT concentrate appears to be well incorporated, with no observable agglomerates in the drawdown, and only a few small features are observed in micrographs at 100× and 1000× (**Figure 1c**). These features are smaller than the nozzle diameter of the printer and thus are expected to have minimal effect on the printing. For 3D printing ESD materials, this extent of mix is sufficient to prevent issues with print nozzle clogging.

Along with visual inspection, the extent of dispersion was also checked by measuring the resistance of the resin after each mix cycle. Evenly distributed conductive networks are formed as the filler is dispersed, resulting in a decrease in the material's overall resistance as measured by an ohmmeter. The resistance of the resin decreased significantly from >2 MΩ after the first mix to 1 kΩ to 2 kΩ by the third mix. The resistance remained stable after the fourth mix, obtaining a value that does not change by more than 7% after subsequent mixing (**Figure 2d**).

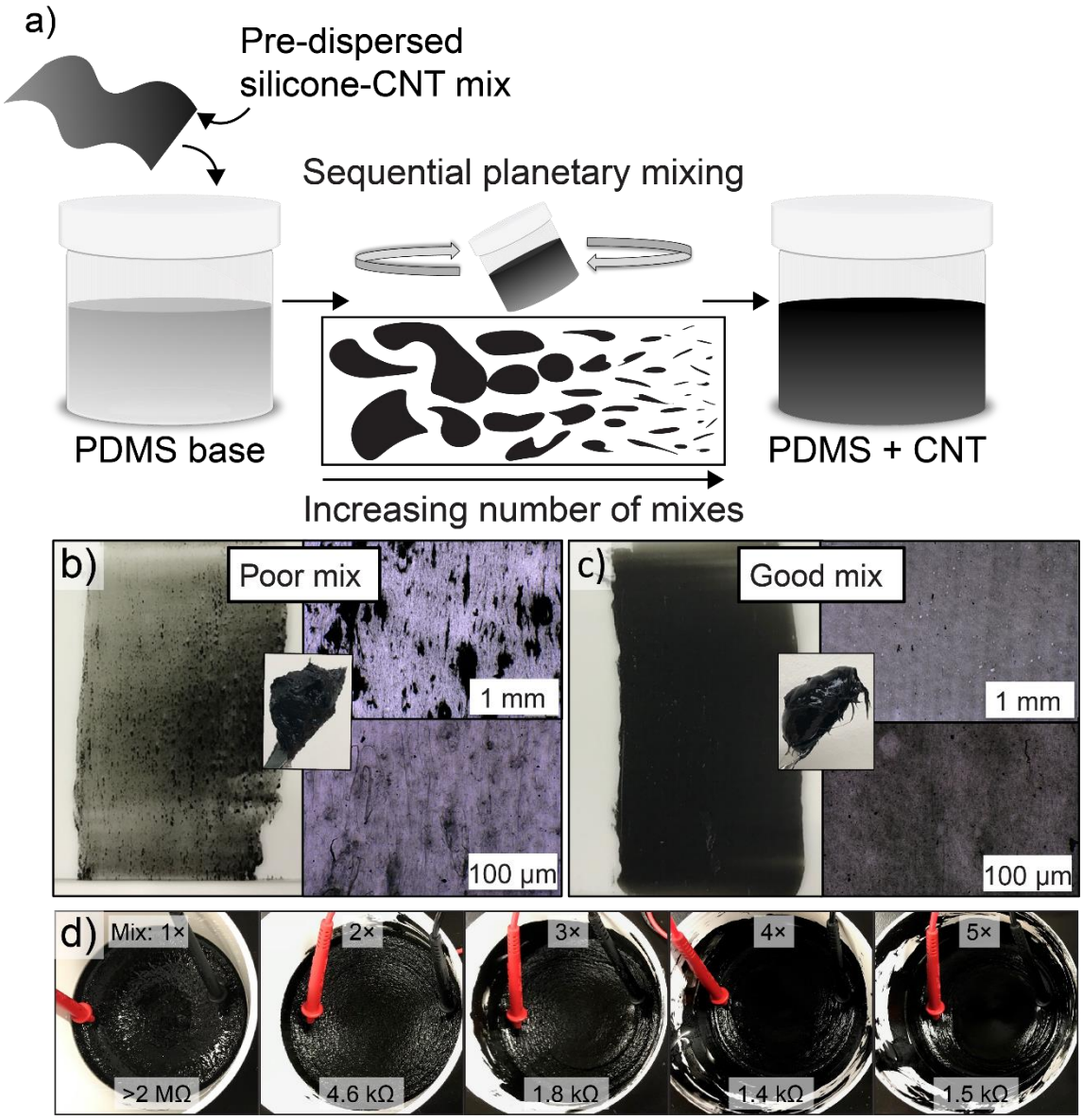

Figure 2. Dispersion of CNT mixture into silicone polymer via sequential planetary mixing. (a) Schematic of mixing process. (b) Images of 10 µm drawdowns at 1×, 100×, and 1000× magnification with inset image of mixed ink after one mix; results in poor dispersion. (c) Images of 10 µm drawdowns at 1×, 100×, and 1000× magnification with inset image of mixed ink after five mixes; results in good dispersion. (d) Ohmmeter resistance measurements of first mix > 2 x 10^6 Ω, second mix = 4.6 x 10^4 Ω, third mix = 1.8 x 10^4 Ω, fourth mix = 1.4 x 10^4 Ω, fifth mix = 1.5 x 10^4 Ω show a decrease in resistance up to three mixes due to improving incorporation of conductive CNT filler into polymer matrix after each mix.

2.2 Resin rheological properties and cured mechanical properties

Next, we examined the effect of CNT concentration on the rheological and mechanical properties since increased concentrations of CNTs may stiffen soft materials.[57,58] The rheological properties of uncured formulations were measured (**Figure 3a,b**) to evaluate the yield stress and

plateau storage modulus, which are important properties that dictate filament sagging and extrusion. The plateau storage modulus is represented by the storage modulus at 20 Pa, and the yield stress was determined as the interpolated oscillation stress when the loss modulus exceeded the storage modulus as the formulation yielded. While typical custom formulations that we produce contain high loadings of silica (>25 wt. %), we first focus on formulations that contain 15 wt. % silica to demonstrate the need to consider the balance between silica content and CNT content in formulating for printing (**Figure 3a**). At 15 wt. % silica and 0 wt. % CNT, the formulation reaches a yield stress of 127 Pa and a plateau storage modulus of 0.0065 MPa. These values are well below those that were previously demonstrated as suitable for printing gap-spanning structures.[13] As the CNT concentration is increased to 0.25 wt. %, the yield stress and plateau modulus increase modestly to 282 Pa and 0.018 Pa, respectively. At 2.5 wt. % CNT, the yield stress and plateau modulus reach 6394 Pa and 0.13 MPa, which is appropriate for printing structures that span gaps; however, the conductivity of this composite is increased to beyond what is suitable for ESD.

Thus, our formulating approach must balance CNT concentration with silica loading to achieve printability while reaching the conductivity needed for ESD. For a silicone formulation with 30 wt. % silica that does not contain CNT, the plateau storage modulus is 0.19 MPa, and the yield stress is 1549 Pa. As the CNT concentration increased from 0.1 wt. % to 0.5 wt. %, the plateau storage modulus and yield stress increased monotonically, reaching a plateau storage modulus of 0.25 MPa and a yield stress of 1811 Pa at 0.5 wt. % CNT (**Figure 3c**). These properties are moderately increased but remain within the range of printability with our DIW setup. The effects of the HMDZ-treated silica, which is loaded to 30 wt. % in the formulation, along with the

associative thickening effects of the silicone polyether thixotropic additive dominate the rheological properties.[13,15,16]

We then measured the hardness, compression set, and tensile mechanical properties of molded composites to evaluate mechanical properties that may be of interest for porous printed structures. An increase in the CNT concentration resulted in an increase in Shore hardness. The hardness of the silicone that does not contain CNT is Shore 55 A, and the hardness increased to Shore 57, 61, and 63 A for 0.1, 0.25, and 0.5 wt. % CNT respectively (**Figure 3d**). An increase in hardness is expected due to the inclusion of the rigid CNTs; however, the increases are moderate and within the range of values that are typical for common silicone materials. For all formulations, the compression set remained low (below 5%), which indicates promise for maintaining load retention over time. The tensile mechanical properties were also measured and were consistent with trends observed for the hardness measurements. Represented by the secant modulus at 50% strain, the incorporation of CNTs resulted in stiffening (**Figure 3e**). For silicone that does not contain CNT, the secant modulus at 50% strain is 2500 kPa, increasing to 5000 kPa at 0.5 wt. % CNTs. Overall, these mechanical properties remain suitable for applications that require the mechanical properties of silicones without CNTs despite slight increases in hardness and secant modulus.

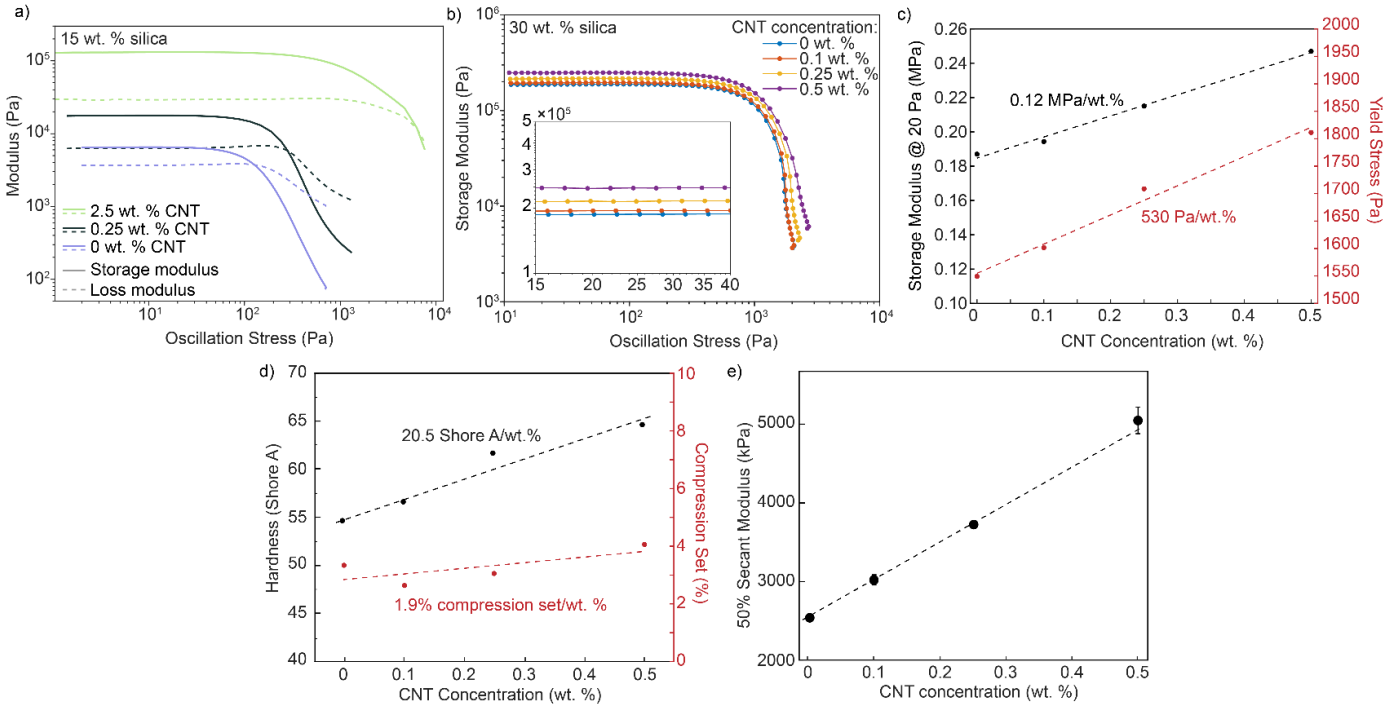

Figure 3. The effect of adding incremental loading of CNT concentrate to silicone dispersions on rheological and mechanical behavior. (a) Oscillatory rheology tests of storage and loss modulus as a function of CNT loading when incorporating 15 wt. % silica. Note that at 2.5% CNT, the formulation achieves high yield stress but is not suitable for ESD due to high conductivity. (b) Oscillatory rheology test of storage modulus with concentrate loading. (c) Rheology testing shows increase of storage modulus at 20 Pa oscillatory stress and an increase in yield stress (d) Testing of cured specimens demonstrating a stable compression set and slight increase in hardness with loading. (e) 50% secant tensile modulus increases with the addition of CNT concentrate. Dashed lines show linear trends with CNT concentration, along with their corresponding slope values.

2.3 Printed materials characterization

Once the base material was characterized, samples with lattice architectures were printed in a helicoidal pattern where each layer was offset by 60° from the previous and then cured. Cross section imaging of the resulting printed lattice structure shows a regular periodic spacing of strands (**Figure 4a, Video S2**). The printed foam can be elastically deformed under a compressive stress and returns to its original shape after compression (**Figures 4b-d**). The periodic spacing between strands allows for good compressibility. The load deflection stress-strain response of printed lattices with varying loading of CNT were compared (**Figure 4e**). At lower strains, up to around 0.2 mm/mm, samples had similar strain responses. At higher strains, materials with a higher filler loading demonstrate a slightly stiffer response compared to the silicone without CNTs, as expected

from the mechanical data. Overall, the printed structure permits compressibility while the inclusion of CNTs has a minimal impact on the mechanical properties of printed structures.

Strand diameters for bottom, middle, and top strands of printed specimens were measured and compared as a function of CNT loading (**Figure 4f,g**). Generally, middle strands appear to have a slightly larger diameter than the bottom and top strands, although the differences are on the order of microns. Across formulations with varying CNT loadings, strand diameters appear relatively similar up to 0.25 wt. % CNT loading, but appear to decrease slightly at 0.5 wt. % loading. Overall, these metrological characterizations highlight the fidelity of the printing process across the different CNT concentrations.

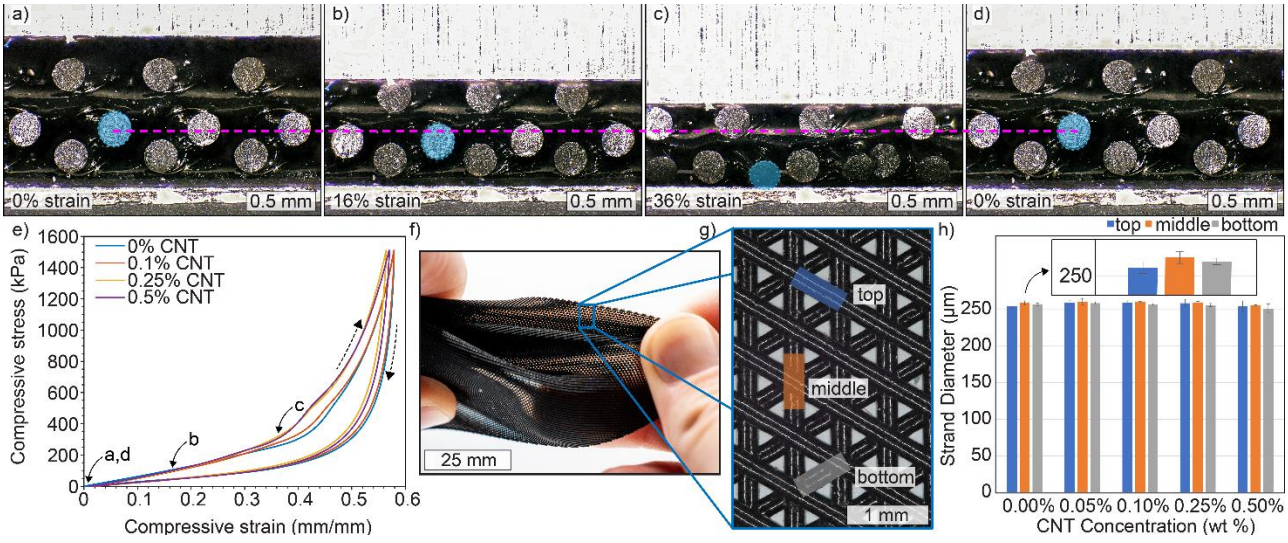

Figure 4. Characterization of printed composites. (a-d) A cross section of the printed ESD silicone was compressed between two parallel plates (lighter color in photographs. a-c) and then allowed to return to 0% strain. (e) The compressive properties were measured; the equivalent cross section images are indicated in the graph. The loading and unloading of compression is indicated on the graph. (f,g) Printed structures were characterized by measuring the strand size. (h) The strand size remained fairly consistent across the range of measured compositions. The inset shows a zoomed view of the bar graph for one composition.

2.4 ESD properties

We then investigated the electrical properties of cured materials filled with CNT concentrate using an electrical test cell connected to a megohmmeter to develop an understanding

of the material's ability to dissipate charge. The addition of small amounts of CNT, up to 0.1 wt. %, reduces the volumetric and surface resistivity of cast sheets by a factor of 10^6-10^7 (**Figure 5a,b**). Note that the megohmmeter range is limited to measurements as low as 1 kΩ, and electrostatic dissipation transitions to conduction as the volume or surface resistivity reach 10^6 Ω cm or Ω/sq. Values below 10^6 Ω cm or Ω/sq may be considered irrelevant for our application. As the CNT concentration reaches 0.25 wt. %, the volume and resistivity begin to decrease below 10^6 Ω cm and Ω/sq. These values do not change as the CNT concentration increased to 0.5 wt. %; however, this trend appears to be related to the experimental setup (e.g., due to effects of contact resistance) as measurements with a handheld ohmmeter showed larger differences between 0.25 and 0.5 wt. % CNT when compared to the megohmmeter.

As opposed to the bulk sheets, the surface resistivity of printed foams remains high at 0.1 wt. % CNT, around 10^{14} Ω/sq on both the top and bottom of the printed part. With the addition of 0.25 wt. % CNT, the surface resistivity drops by a factor of 10^6 down to 10^8 Ω/sq. Loading up to 0.5 wt. % CNT decreases the surface resistivity slightly, around another ≈10× to 100× depending on the side tested (**Figure 5c**). For all CNT concentrations, the surface resistivity is lower when measured on the bottom of the printed sample when compared to the top. This difference may be due to the increased surface contact between the electrodes with the bottom of the print, which is partially flattened from the surface of the print bed during deposition and cure (**Figure 5c, inset**).

To illustrate the dissipative properties, 0 and 0.25 wt. % CNT silicones were brought in contact with a latex surface to introduce charges through triboelectrification onto the specimen surfaces. An electrostatic meter was then used to measure the surface charges remaining on the surface. In the sample without CNTs, the residual surface charge was 8.2 kV, whereas the residual surface charge of the CNT sample was -0.06 kV (**Figure 5d, Video S3**). These results indicate that

charges were trapped on the highly dielectric surface of the silicone without CNTs print, whereas the CNT loaded sample dissipated charges introduced to the material surface, facilitated by the added carbon filler network.

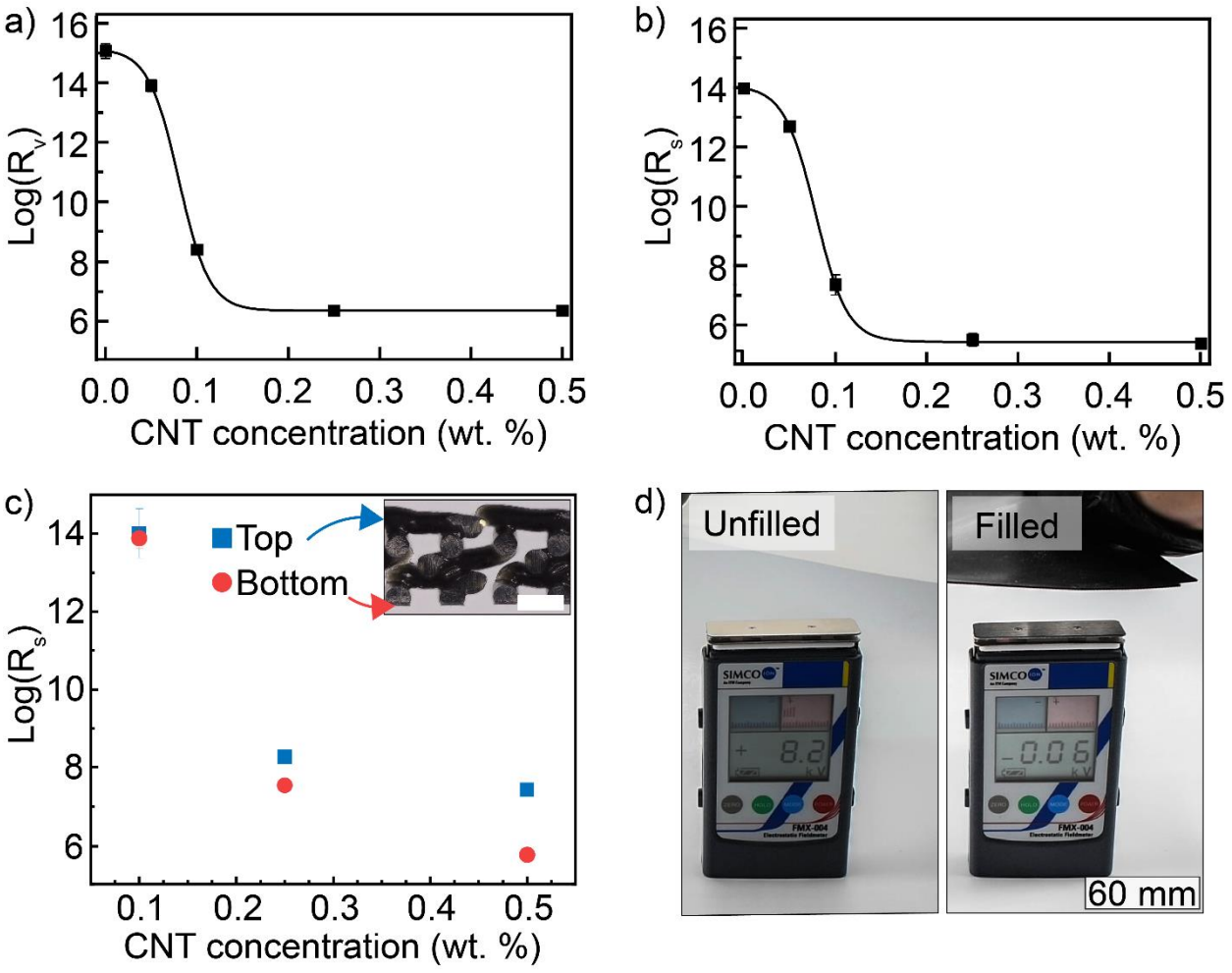

Figure 5. Electrical testing of CNT-loaded silicones. (a) The log of the volumetric resistivity (ohm cm) of a cast 2 mm sheet as a function of CNT loading. (b) The log of the surface resistivity (ohm/sq) of a cast 2 mm sheet as a function of CNT loading. (c) The log of the surface resistivity (ohm/sq) of 60° helicoidal printed sheets as a function of CNT loading measured on top and bottom of printed sheets. The inset shows a cross-section of a printed sheet with top and bottom surfaces labeled. The bottom surface of the print is flat due to curing on the print bed, which may result in an increased surface area contact with the test electrodes. The scale bar is 500 µm. (d) Surface charge measurements of CNT-free and 0.25 wt. % CNT loaded silicone after bringing the print surfaces in contact with a latex surface. The unloaded sample has a measured charge of 8.2 kV, whereas the filled 0.25 wt. % CNT print had a measured charge of -0.06 kV.

Table 1. Rheological, mechanical, and electrical Properties of CNT-Loaded Silicones. Measured R_v values are Ω cm and R_s values are Ω/sq.

CNT wt%	Plateau Storage Modulus (MPa)	Durometer (Shore A)	Secant Modulus (kPa)	Compression Set (%)	Log(R_v)	Log(R_s)
0	0.19	55	2539 ± 14	3.3	15.08 ± 0.25	13.98 ± 0.16
0.1	0.19	57	3016 ± 65	2.6	8.39 ± 0.10	7.37 ± 0.34
0.25	0.22	61	3732 ± 7	3.1	6.33 ± 0.09	5.52 ± 0.22
0.5	0.25	63	5038 ± 170	4	6.33 ± 0.06	5.39 ± 0.04

We further characterized the electrostatic charge transfer of printed silicones with and without CNT using a Faraday cup[59,60] after triboelectric charging with aluminum, cotton, and nylon. Silicone rubber is low on the triboelectric series, so it is highly susceptible to receiving negative charges from materials higher on the series.[61–63] Testing using a Faraday cup indicates an average charge of 200–300 nC for CNT-free prints and 40–150 nC for CNT-filled prints, indicating a 2-3× higher charge transfer in the CNT-free system for all tested materials (**Figure 6a**).

With the Faraday Cup assembly capacitance (C) measured at 170.55 pF, electrostatic voltage potentials (V) were calculated given V = Q/C, where Q is the measured charge. CNT-free prints showed voltage potentials of 1–2 kV, while CNT-filled prints ranged from 0.2–0.8 kV, depending on the triboelectric material used for charging (**Figure 6b**). Between triboelectric materials, cotton and nylon imparted similar charges, while aluminum resulted in slightly lower charge accumulation. These results indicate that CNT-filled prints generate smaller electrostatic potentials compared to CNT-free prints after triboelectric charging with common materials, thus

being better for use with sensitive circuitry.

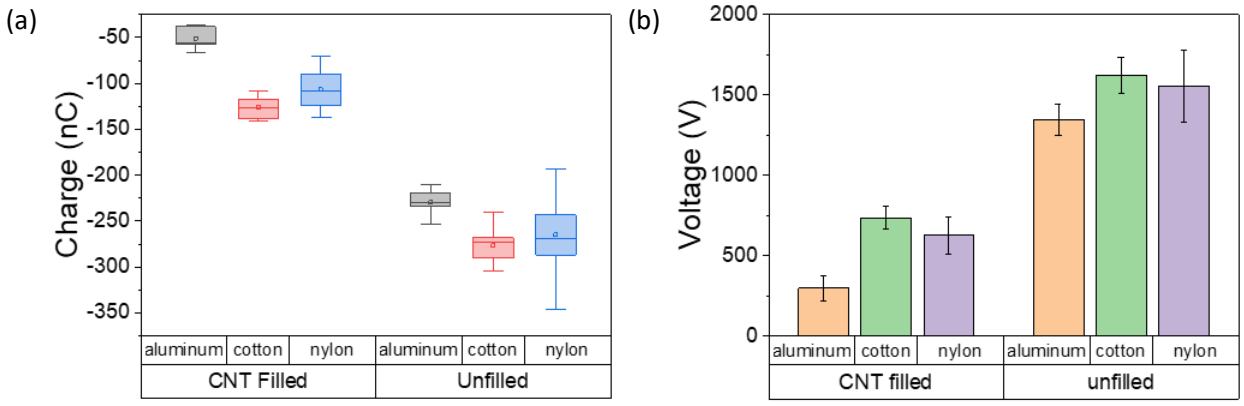

Figure 6. Electrostatic charge transfer testing Faraday Cup (a) Insertion charge values for printed foams with 0.25 wt % CNT and with no CNT after being charged with various triboelectric materials: aluminum, cotton, and nylon. (b) The resulting potential from each measured electrostatic charge given $C_{faraday\ cup}$ = 170.55 pF.

After demonstrating that the incorporation of the CNT concentrate enables dissipative properties without modifying the printability and material properties beyond application requirements (**Table 1)**, we sought to demonstrate potential utility of this composite. This demonstration takes advantage of a key benefit of DIW, which is the ability to print custom conforming structures directly atop components of interest. A circuit board was scanned using a structured light scanner to generate a set of data points that represent the 3-dimensional object, i.e., a point cloud. This point cloud (**Figure 7a**) will support adjustments to the toolpath by enabling a precise calibration of the print surface. The part model is then processed into a toolpath using a general slicer as if it was on a flat substrate.

The cushion was then printed over a portion of the circuit board and sequentially mapped as a point cloud to visualize the printed structure (**Figure 7b**). Defects in the printed structure were apparent (**Figure 7c,** Figure 1e); for example, many of the upper strands did not deposit along an intended straight path. This issue was due in part to the fact that printing height increased slightly

upon each layer affecting final placement of the upper strands. The challenge is the vertical features of the circuit board; printing atop components of interest is more feasible with finer gradient changes in the vertical dimension. Improvements will be made in future iterations; however, the printed structure still functions as intended. In addition to the electrostatic dissipative properties of the composite, the printed structure can also act as a cushion, which is illustrated by striking the circuit board with a hammer (**Figure 7c, Video S4**).

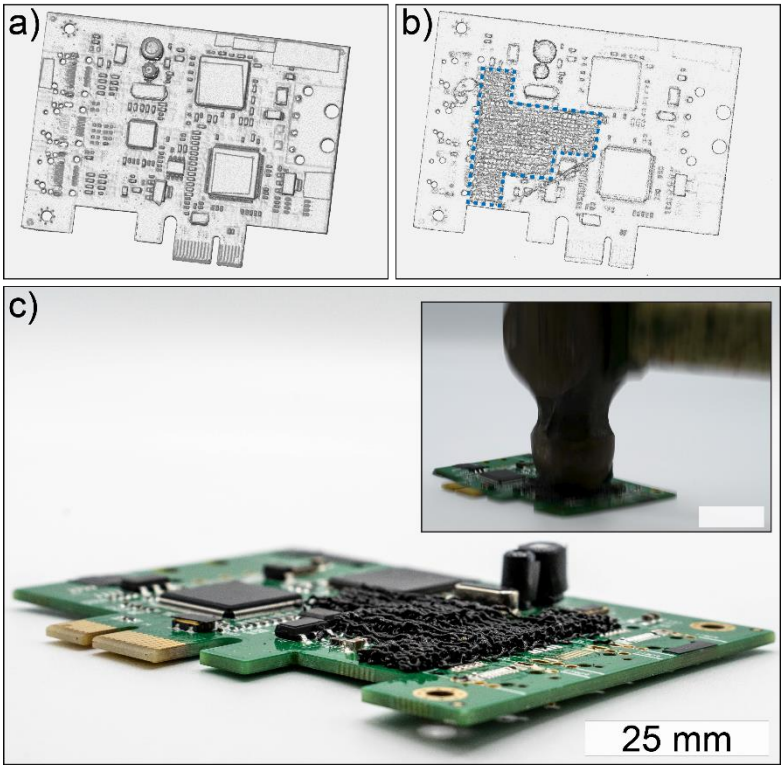

Figure 7. (a) Point cloud of circuit board generated from surface scan before printing. (b) Point cloud of circuit board with printed structure on top. The blue dashed outline highlights the printed portion. (c) Photograph of printed structure atop a circuit board. The inset shows a hammer striking the printed structure. The scale bar in the inset is 25 mm.

3. CONCLUSION:

The incorporation of CNTs into a silicone elastomer can enable electrostatic dissipative properties along with printability for DIW. The hierarchy of the structure, including the print architecture and the CNT morphology, influences the overall properties. Importantly, the CNT

content must be optimized to minimize negative externalities related to the properties of the printable, uncured precursor as well as the final cured composite. Overall, we found that the amount of CNT needed to induce electrostatic dissipation overlaps with the amount of CNT that does not drastically change printability as well as mechanical properties of the final material. Thus, the material can be printed into composite structures with electrostatic dissipative properties. As a demonstration, we printed a structure atop a circuit board. This structure provides unique packaging capabilities, as it can exhibit cushioning as well as electrostatic dissipation as long as it is connected to an appropriate ground. Such packaging capabilities may be important and useful for specialized equipment like those used in medical, robotic, and other applications.

4. EXPERIMENTAL METHODS:

The silicone formulations that are used are based upon previous studies.[64] Briefly, vinyl-terminated silicone macromers (Gelest, Nusil) were mixed with a divinyltetramethyldisiloxane-Pt complex catalyst along with Evonik Aerosil R8200, which is a hexamethyldisilazane (HMDZ)-treated fumed silica, and a polyether siloxane copolymer thixotropic agent (BLUESIL THIXO ADD 22646) to form a part A precursor. The part B precursor contained vinyl-terminated silicone macromers along with a silane-functionalized silicone macromer used for crosslinking (HMS-H271, Gelest) and a Pt inhibitor (1-Ethynyl-1-cyclohexanol, ETCH). The compositions of the Part A precursor and Part B precursor are listed in Table 2 and Table 3, respectively. The total molar ratio of silane to vinyl in a final resin that is mixed from parts A and B was about 2:1. The CNT concentrate consisted of Tuball Matrix 602 (TM 602, OCSiAl), which is a commercial pre-dispersed concentrate consisting of 10 wt. % single walled CNT incorporated into a vinyl-terminated polydimethylsiloxane resin (0.36 mmol vinyl equivalent per gram of polymer). CNT-loaded formulations were made by mixing silicone base resins with varying loading of TM 602 up

to 5 wt. % and then subsequently adding in the part B precursor which contains the HMS H271 crosslinker. To prepare resins for printing, inks were filtered through a 140 μm mesh filter into 30 mL Nordson syringe barrels and centrifuged under vacuum to remove any entrapped air. A Nordson flat-ended piston was inserted to seal the rear of the syringe. Photographs and videos were taken with a Nikon D750 and processed (color and lighting corrections) globally using Adobe Lightroom.

Table 2. Composition of Part A Precursor

Component	Composition	Units
Nusil PLY3-7560	66.99	wt. %
Pt-PL (Catalyst Blend)*	13.19	ppm Pt
Evonik Aerosil R8200	32.16	wt. %
Bluesil Thixo Add 22646	0.27	wt. %

*Mixture of nine parts Nusil PLY2-7560 by weight with one part of divinyltetramethyldisiloxane-Pt complex catalyst (by weight)

Table 3. Composition of Part B Precursor

Component	Composition	Units
Gelest HMS-H271	45	wt. %
Gelest DMS-V05	27	wt. %
ETCH-PL (Inhibitor Blend)*	6000	ppm ETCH
Nusil PLY3-7560	22	wt. %

*Mixture of nine parts Nusil PLY2-7560 by weight with one part 1-ethynyl-1-cyclohexanol (by weight)

Mixing Studies

Resins were mixed using a Thinky ARV-310 planetary mixer with vacuum capability. Each mixing step was at 2,000 rpm for 1 minute. Between centrifugal mixing, resins were hand mixed using a stainless steel spatula to assist with incorporation. A 10 μm Mayer drawdown rod was used to form a thin film on glass slides, and a Keyence VHX-7000 series microscope was used to take

transmitted light images of drawdown samples to check extent of CNT dispersion. A digital ohmmeter was also used to measure resistance of the mix to determine extent of CNT incorporation.

Rheological Testing

Yield stress and storage modulus was obtained with a HR-3 rheometer (TA Instruments) equipped with a 20 mm crosshatched stainless steel plate. Samples were stressed under an oscillatory stress sweep at a frequency of 1 Hz. Resulting profile was processed in Trios software v4.5.0.42498 (TA Instruments).

Compression Set and Durometer

Relative compression values were obtained on cured pucks following ASTM 395, Test Method B. Resins were transferred into a steel mold and cured at 150 °C for 16 hours to form pucks with a nominal thickness of 12.5 mm and diameter of 29 mm. Sample durometers were measured on cured compression set pucks using a Shore A durometer hardness meter. The thicknesses of the original specimens are measured using an MTG digital thickness gauge. The specimens were then placed between spacers in the compression device and compressed to 25% of their original height. The compressed samples were transferred into a nitrogen purged oven held at 70 °C for 70 hours. After removing specimens from oven, they were allowed to cool for 30 minutes, and then the final thickness was measured.

Tensile Testing

Tensile tests were run following ASTM D638 using Type IV dogbones cut from 2 mm sheets cast in an ASTM D3182 mold and cured at 150 °C for 16 hours. Tests were run using an Instron 5967 equipped with a 100 N load cell and pneumatic grips set to a pressure of 50 psi. Tensile specimens were stretched at 500 mm/min until failure.

Printing

Syringes loaded with silicone-based inks were affixed to the z-axis of an Aerotech xy movement stage controlled via an Npaq controller through an Aerotech CNC operator interface. A positive-displacement dispenser (Aerotech BM200-D25-E1000H-15 motor driving a Parker ETH032M05A1PANFMN0150A linear actuator) supplied displacement to extrude ink through a 250 μm nozzle to yield a nominal 250 μm strand size. G-code was implemented into the Aerotech software to generate the printed structures (e.g., a 5 layered 8-inch square with a strand spacing of 585 μm, z-height of 225 μm, and a 60° helicoidal print shown in Figure 4). The printed flats were cured using a 1-hour ramp to 150 °C then a 16 hour hold at 150 °C in an oven.

For printing atop a circuit board, the board was first adapted for scanning and printing by desoldering larger components on the underside. The removal of these components helps to level the board to form a more suitable printing surface as part of our demonstration. A contour bracket of the circuit board was designed and 3D printed, allowing for repeated zeroing on a substrate. We apply corrections derived from our point cloud to the coordinate commands of a flat toolpath. These adjustments form discretized coordinates that can cause fast erratic movements in varying height areas, affecting the ink to be deposited as well as accelerations. Implementation of sloped ramps for higher positions with finer resolution in toolpath resolved part of this issue.

Electrical characterization

Resistivity measurements were performed on casted 2 mm sheets and printed sheets using an IET Labs 1865+ Megohmmeter with a 1865-11 test cell. Tests were run using a 5 V applied voltage. Measurement times were set to 60 s and sampling number to average was set to 50. The test cell was calibrated beforehand to subtract out any current leakage from cables and the test cell.

Both surface and volume resistivity were measured on the samples in triplicate. To demonstrate electric dissipation, a piezoelectric device was used to induce a charge into the material. A Simco-Ion FMX-004 electrostatic field meter was used to measure the surface charges remaining on sample surfaces after triboelectrification from a latex sample. Samples were handled using nitrile gloves.

Charge transfer measurements were taken using a 20-gallon medium sized Faraday cup. Electrostatic charges from the samples transferred to the Faraday Cup were measured using an ETS Model 230 nanocoloumb meter. The capacitance for the Faraday Cup setup was measured using a GLK Instruments Model 3000 digital capacitance meter. Printed samples were charged through triboelectrification by rubbing and compressing on aluminum, cotton, and nylon surfaces multiple times before each test. The test was run in a temperature and humidity controlled atmosphere targeted to a relative percent humidity of less than 15 % at 20 °C.

ASSOCIATED CONTENT

Supporting Information.

The following files are available free of charge.

- Supplementary Video S1-S4 – S1: Visualization of electric shock; S2: Compression of printed structure; S3: Measurement of electrostatic dissipation properties; S4: Striking printed structure with high impact force.

AUTHOR INFORMATION

Corresponding Author

Jeremy Armas – *Materials Science Division, Lawrence Livermore National Laboratory, Livermore, CA 94550, United States.* Email: armas3@llnl.gov

Author Contributions

J.M.L., M.J.F., C.K.L., and J.A.A conceived ideas and supervised experiments. J.A.A. developed formulations, measured print structure dimensions, characterized compression set, and characterized material resistivity. J.A.A., C.K.L, and L.X.P.P. developed and characterized mixing procedure. J.A.A., S.S., and M.J.F. formulated materials and characterized rheological properties. J.A.A. and M.J.F. characterized load deflection response of printed structures, characterized electrostatic charge using electrostatic field meter, and captured images and videos. K. P. F. and T. H. scanned, developed the toolpath, and printed the structure on the circuit board demonstrator. S.F.W. characterized the electrostatic properties of printed materials using Faraday cup testing. K. L. B., F.X., and T.M.B. characterized tensile properties and compression set. J.A.A., M.J.F., and S.S. wrote the manuscript. All authors discussed and edited the manuscript.

ACKNOWLEDGMENT

This work was performed under the auspices of the U.S. Department of Energy by Lawrence Livermore National Laboratory under Contract DE-AC52-07NA27344, LLNL-JRNL-865276.

REFERENCES

(1) Adams, J. J.; Duoss, E. B.; Malkowski, T. F.; Motala, M. J.; Ahn, B. Y.; Nuzzo, R. G.; Bernhard, J. T.; Lewis, J. A. Conformal Printing of Electrically Small Antennas on Three-Dimensional Surfaces. *Advanced Materials* **2011**, *23* (11), 1335–1340. https://doi.org/10.1002/adma.201003734.

(2) Nguyen, D.; Murialdo, M.; Hornbostel, K.; Pang, S.; Ye, C.; Smith, W.; Baker, S.; Bourcier, W.; Knipe, J.; Aines, R.; Stolaroff, J. 3D Printed Polymer Composites for CO2 Capture. *Ind. Eng. Chem. Res.* **2019**, *58* (48), 22015–22020. https://doi.org/10.1021/acs.iecr.9b04375.

(3) Zhu, C.; Liu, T.; Qian, F.; Han, T. Y.-J.; Duoss, E. B.; Kuntz, J. D.; Spadaccini, C. M.; Worsley, M. A.; Li, Y. Supercapacitors Based on Three-Dimensional Hierarchical Graphene Aerogels with Periodic Macropores. *Nano Lett.* **2016**, *16* (6), 3448–3456. https://doi.org/10.1021/acs.nanolett.5b04965.

(4) Tagliaferri, S.; Panagiotopoulos, A.; Mattevi, C. Direct Ink Writing of Energy Materials. *Mater. Adv.* **2021**, *2* (2), 540–563. https://doi.org/10.1039/D0MA00753F.
(5) Ford, M. J.; Porcincula, D. H.; Telles, R.; Mancini, J. A.; Wang, Y.; Rizvi, M. H.; Loeb, C. K.; Moran, B. D.; Tracy, J. B.; Lewis, J. A.; Yang, S.; Lee, E.; Cook, C. C. Movement with Light: Photoresponsive Shape Morphing of Printed Liquid Crystal Elastomers. *Matter* **2024**, *7* (3), 1207–1229. https://doi.org/10.1016/j.matt.2024.01.006.
(6) Shafranek, R. T.; Millik, S. C.; Smith, P. T.; Lee, C.-U.; Boydston, A. J.; Nelson, A. Stimuli-Responsive Materials in Additive Manufacturing. *Progress in Polymer Science* **2019**, *93*, 36–67. https://doi.org/10.1016/j.progpolymsci.2019.03.002.
(7) Loeb, C. K.; Nguyen, D. T.; Bryson, T. M.; Duoss, E. B.; Wilson, T. S.; Lenhardt, J. M. Hierarchical 3D Printed Porous Silicones with Porosity Derived from Printed Architecture and Silicone-Shell Microballoons. *Additive Manufacturing* **2022**, *55*, 102837. https://doi.org/10.1016/j.addma.2022.102837.
(8) Wu, A. S.; Small IV, W.; Bryson, T. M.; Cheng, E.; Metz, T. R.; Schulze, S. E.; Duoss, E. B.; Wilson, T. S. 3D Printed Silicones with Shape Memory. *Sci Rep* **2017**, *7* (1), 4664. https://doi.org/10.1038/s41598-017-04663-z.
(9) Ortiz-Acosta, D.; Moore, T.; Safarik, D. J.; Hubbard, K. M.; Janicke, M. 3D-Printed Silicone Materials with Hydrogen Getter Capability. *Advanced Functional Materials* **2018**, *28* (17), 1707285. https://doi.org/10.1002/adfm.201707285.
(10) Lewicki, J. P.; Rodriguez, J. N.; Zhu, C.; Worsley, M. A.; Wu, A. S.; Kanarska, Y.; Horn, J. D.; Duoss, E. B.; Ortega, J. M.; Elmer, W.; Hensleigh, R.; Fellini, R. A.; King, M. J. 3D-Printing of Meso-Structurally Ordered Carbon Fiber/Polymer Composites with Unprecedented Orthotropic Physical Properties. *Sci Rep* **2017**, *7* (1), 43401. https://doi.org/10.1038/srep43401.
(11) Duoss, E. B.; Weisgraber, T. H.; Hearon, K.; Zhu, C.; Small IV, W.; Metz, T. R.; Vericella, J. J.; Barth, H. D.; Kuntz, J. D.; Maxwell, R. S.; Spadaccini, C. M.; Wilson, T. S. Three-Dimensional Printing of Elastomeric, Cellular Architectures with Negative Stiffness. *Advanced Functional Materials* **2014**, *24* (31), 4905–4913. https://doi.org/10.1002/adfm.201400451.
(12) Maiti, A.; Small, W.; Lewicki, J. P.; Weisgraber, T. H.; Duoss, E. B.; Chinn, S. C.; Pearson, M. A.; Spadaccini, C. M.; Maxwell, R. S.; Wilson, T. S. 3D Printed Cellular Solid Outperforms Traditional Stochastic Foam in Long-Term Mechanical Response. *Sci Rep* **2016**, *6* (1), 24871. https://doi.org/10.1038/srep24871.
(13) Durban, M. M.; Lenhardt, J. M.; Wu, A. S.; Small IV, W.; Bryson, T. M.; Perez-Perez, L.; Nguyen, D. T.; Gammon, S.; Smay, J. E.; Duoss, E. B.; Lewicki, J. P.; Wilson, T. S. Custom 3D Printable Silicones with Tunable Stiffness. *Macromolecular Rapid Communications* **2018**, *39* (4), 1700563. https://doi.org/10.1002/marc.201700563.
(14) Truby, R. L.; Lewis, J. A. Printing Soft Matter in Three Dimensions. *Nature* **2016**, *540* (7633), 371–378. https://doi.org/10.1038/nature21003.
(15) Ramesh, U.; Miller, J.; Stottelmire, B.; Beach, J.; Patterson, S.; Cumming, L.; Torres, S. W.; Even, D.; Dvornic, P.; Berkland, C. PDMS Microspheres as Rheological Additives for PDMS-Based DIW Inks. *Advanced Industrial and Engineering Polymer Research* **2024**. https://doi.org/10.1016/j.aiepr.2024.06.001.
(16) Beach, J.; Mann, S.; Ault, C.; Radojcic, D.; Wan, X.; Zlatanic, A.; Patterson, S.; Messman, J. M.; Dvornic, P. R. "All-in-One" Thixotropic Polysiloxane Pastes for UV-Activated Room

Temperature Hydrosilylation Cross-Linking in Additive Manufacturing. *Macromolecules* **2021**, *54* (4), 1715–1724. https://doi.org/10.1021/acs.macromol.0c02457.

(17) Truby, R. L.; Wehner, M.; Grosskopf, A. K.; Vogt, D. M.; Uzel, S. G. M.; Wood, R. J.; Lewis, J. A. Soft Somatosensitive Actuators via Embedded 3D Printing. *Advanced Materials* **2018**, *30* (15), 1706383. https://doi.org/10.1002/adma.201706383.

(18) Muth, J. T.; Vogt, D. M.; Truby, R. L.; Mengüç, Y.; Kolesky, D. B.; Wood, R. J.; Lewis, J. A. Embedded 3D Printing of Strain Sensors within Highly Stretchable Elastomers. *Advanced Materials* **2014**, *26* (36), 6307–6312. https://doi.org/10.1002/adma.201400334.

(19) Zhou, L.; Gao, Q.; Fu, J.; Chen, Q.; Zhu, J.; Sun, Y.; He, Y. Multimaterial 3D Printing of Highly Stretchable Silicone Elastomers. *ACS Appl. Mater. Interfaces* **2019**, *11* (26), 23573–23583. https://doi.org/10.1021/acsami.9b04873.

(20) Rus, D.; Tolley, M. T. Design, Fabrication and Control of Soft Robots. *Nature* **2015**, *521* (7553), 467–475. https://doi.org/10.1038/nature14543.

(21) Shan, S.; Kang, S. H.; Raney, J. R.; Wang, P.; Fang, L.; Candido, F.; Lewis, J. A.; Bertoldi, K. Multistable Architected Materials for Trapping Elastic Strain Energy. *Advanced Materials* **2015**, *27* (29), 4296–4301. https://doi.org/10.1002/adma.201501708.

(22) Clausen, A.; Wang, F.; Jensen, J. S.; Sigmund, O.; Lewis, J. A. Topology Optimized Architectures with Programmable Poisson's Ratio over Large Deformations. *Advanced Materials* **2015**, *27* (37), 5523–5527. https://doi.org/10.1002/adma.201502485.

(23) Ford, M. J.; Loeb, C. K.; Pérez, L. X. P.; Gammon, S.; Guzorek, S.; Gemeda, H. B.; Golobic, A. M.; Honnell, A.; Erspamer, J.; Duoss, E. B.; Wilson, T. S.; Lenhardt, J. M. 3D Printing of Transparent Silicone Elastomers. *Advanced Materials Technologies* **2022**, *7* (5), 2100974. https://doi.org/10.1002/admt.202100974.

(24) Tugui, C.; Cazacu, M.; Manoli, D. M.; Stefan, A.; Duduta, M. All-Silicone 3D Printing Technology: Toward Highly Elastic Dielectric Elastomers and Complex Structures. *ACS Appl. Polym. Mater.* **2023**, *5* (10), 7936–7946. https://doi.org/10.1021/acsapm.3c01190.

(25) Kim, Y.; Yuk, H.; Zhao, R.; Chester, S. A.; Zhao, X. Printing Ferromagnetic Domains for Untethered Fast-Transforming Soft Materials. *Nature* **2018**, *558* (7709), 274–279. https://doi.org/10.1038/s41586-018-0185-0.

(26) Valentine, A. D.; Busbee, T. A.; Boley, J. W.; Raney, J. R.; Chortos, A.; Kotikian, A.; Berrigan, J. D.; Durstock, M. F.; Lewis, J. A. Hybrid 3D Printing of Soft Electronics. *Advanced Materials* **2017**, *29* (40), 1703817. https://doi.org/10.1002/adma.201703817.

(27) Guo, S.-Z.; Qiu, K.; Meng, F.; Park, S. H.; McAlpine, M. C. 3D Printed Stretchable Tactile Sensors. *Advanced Materials* **2017**, *29* (27), 1701218. https://doi.org/10.1002/adma.201701218.

(28) Fekiri, C.; Kim, H. C.; Lee, I. H. 3D-Printable Carbon Nanotubes-Based Composite for Flexible Piezoresistive Sensors. *Materials* **2020**, *13* (23), 5482. https://doi.org/10.3390/ma13235482.

(29) Ford, M. J.; Patel, D. K.; Pan, C.; Bergbreiter, S.; Majidi, C. Controlled Assembly of Liquid Metal Inclusions as a General Approach for Multifunctional Composites. *Advanced Materials* **2020**, *32* (46), 2002929. https://doi.org/10.1002/adma.202002929.

(30) Luo, B.; Wei, Y.; Chen, H.; Zhu, Z.; Fan, P.; Xu, X.; Xie, B. Printing Carbon Nanotube-Embedded Silicone Elastomers via Direct Writing. *ACS Appl. Mater. Interfaces* **2018**, *10* (51), 44796–44802. https://doi.org/10.1021/acsami.8b18614.

(31) Shar, A.; Glass, P.; Park, S. H.; Joung, D. 3D Printable One-Part Carbon Nanotube-Elastomer Ink for Health Monitoring Applications. *Advanced Functional Materials* **2023**, *33* (5), 2211079. https://doi.org/10.1002/adfm.202211079.
(32) Balberg, I.; Anderson, C. H.; Alexander, S.; Wagner, N. Excluded Volume and Its Relation to the Onset of Percolation. *Phys. Rev. B* **1984**, *30* (7), 3933–3943. https://doi.org/10.1103/PhysRevB.30.3933.
(33) Li, J.; Ma, P. C.; Chow, W. S.; To, C. K.; Tang, B. Z.; Kim, J.-K. Correlations between Percolation Threshold, Dispersion State, and Aspect Ratio of Carbon Nanotubes. *Advanced Functional Materials* **2007**, *17* (16), 3207–3215. https://doi.org/10.1002/adfm.200700065.
(34) Choi, H.-J.; Kim, M. S.; Ahn, D.; Yeo, S. Y.; Lee, S. Electrical Percolation Threshold of Carbon Black in a Polymer Matrix and Its Application to Antistatic Fibre. *Sci Rep* **2019**, *9* (1), 6338. https://doi.org/10.1038/s41598-019-42495-1.
(35) Baughman, R. H.; Zakhidov, A. A.; de Heer, W. A. Carbon Nanotubes--the Route Toward Applications. *Science* **2002**, *297* (5582), 787–792. https://doi.org/10.1126/science.1060928.
(36) Rousseaux, D.; Lhost, O.; Lodefier, P. Industrial Advanced Carbon Nanotubes-Based Materials for Electrostatic Discharge Packaging. In *2013 14th International Conference on Electronic Packaging Technology*; 2013; pp 386–388. https://doi.org/10.1109/ICEPT.2013.6756495.
(37) Wang, J.; Chang, A. S. P.; Hunter, S. L.; Golobic, A. M.; Sherfield, S. N.; Lenhardt, J. M.; Duoss, E. B.; Matthews, M. J. Development of the Multi-Material Inspection for Closed-Loop Rapid Optimization (MICRO) Sensor for Extrusion-Based Additive Manufacturing of Metal-Polymer Composite Inks. *IEEE Sensors Journal* **2021**, *21* (1), 265–272. https://doi.org/10.1109/JSEN.2020.3014790.
(38) *Electrostatic Discharge*, 1st ed.; John Wiley & Sons, Ltd, 2009. https://doi.org/10.1002/9780470495070.
(39) Floyd, H. L. Electric Shock Injuries from Static Electricity Discharges. In *2011 IEEE IAS Electrical Safety Workshop*; 2011; pp 1–3. https://doi.org/10.1109/ESW.2011.6164721.
(40) McClure, R.; Britton, L.; Holmstrom, D.; Kaszniak, M. Static Electric Discharge during Solvent Handling and Storage; 2009.
(41) Tamminen, P.; Ukkonen, L.; Sydänheimo, L. Correlation of Component Human Body Model and Charged Device Model Qualification Levels with Electrical Failures in Electronics Assembly. *Journal of Electrostatics* **2016**, *79*, 38–44. https://doi.org/10.1016/j.elstat.2015.12.002.
(42) Lai, T.-H.; Ker, M.-D.; Chang, W.-J.; Tang, T.-H.; Su, K.-C. High-Robust ESD Protection Structure with Embedded SCR in High-Voltage CMOS Process. In *2008 IEEE International Reliability Physics Symposium*; 2008; pp 627–628. https://doi.org/10.1109/RELPHY.2008.4558959.
(43) Amerasekera, E. A.; Duvvury, C. *ESD in Silicon Integrated Circuits*, 2nd edition.; Wiley: Chichester, 2002.
(44) Duvvury, C.; Rountree, R. N.; McPhee, R. A. ESD Protection: Design and Layout Issues for VLSI Circuits. *IEEE Transactions on Industry Applications* **1989**, *25* (1), 41–47. https://doi.org/10.1109/28.18867.
(45) *EOS/ESD Fundamentals | EOS/ESD Association, Inc.* https://www.esda.org/esd-overview/esd-fundamentals/ (accessed 2024-07-24).

(46) *Control of Surface Charges by Radicals as a Principle of Antistatic Polymers Protecting Electronic Circuitry | Science*. https://www.science.org/doi/10.1126/science.1241326 (accessed 2024-07-29).
(47) Angelopoulos, M. Conducting Polymers in Microelectronics. *IBM Journal of Research and Development* **2001**, *45* (1), 57–75. https://doi.org/10.1147/rd.451.0057.
(48) Jane, M. Characterization of Electrically Conductive 3D Printing Materials for Use in ESD Control Programs. *2022 44th Annual EOS/ESD Symposium (EOS/ESD)* **2022**, 1–10. https://doi.org/10.23919/EOS/ESD54763.2022.9928455.
(49) Guo, B.; Ji, X.; Wang, W.; Chen, X.; Wang, P.; Wang, L.; Bai, J. Highly Flexible, Thermally Stable, and Static Dissipative Nanocomposite with Reduced Functionalized Graphene Oxide Processed through 3D Printing. *Composites Part B: Engineering* **2021**, *208*, 108598. https://doi.org/10.1016/j.compositesb.2020.108598.
(50) Arigbabowo, O. K.; Tate, J. S. Additive Manufacturing of Polyamide Nanocomposites for Electrostatic Charge Dissipation Applications. *Materials Science and Engineering: B* **2021**, *271*, 115251. https://doi.org/10.1016/j.mseb.2021.115251.
(51) Jr, W. J. S.; Zhang, S. Thickening Silicones with Elastomeric Silicone Polyethers. US5811487A, September 22, 1998. https://patents.google.com/patent/US5811487A/en (accessed 2024-07-10).
(52) Zhang, G.-D.; Wu, J.-R.; Tang, L.-C.; Li, J.-Y.; Lai, G.-Q.; Zhong, M.-Q. Rheological Behaviors of Fumed Silica/Low Molecular Weight Hydroxyl Silicone Oil. *Journal of Applied Polymer Science* **2014**, *131* (17). https://doi.org/10.1002/app.40722.
(53) Sarmah, A.; Desai, S. K.; Crowley, A. G.; Zolton, G. C.; Tezel, G. B.; Harkin, E. M.; Tran, T. Q.; Arole, K.; Green, M. J. Additive Manufacturing of Nanotube-Loaded Thermosets via Direct Ink Writing and Radio-Frequency Heating and Curing. *Carbon* **2022**, *200*, 307–316. https://doi.org/10.1016/j.carbon.2022.08.063.
(54) Yuan, Q. W.; Mark, J. E. Reinforcement of Poly(Dimethylsiloxane) Networks by Blended and in-Situgenerated Silica Fillers Having Various Sizes, Size Distributions, and Modified Surfaces. *Macromolecular Chemistry and Physics* **1999**, *200* (1), 206–220. https://doi.org/10.1002/(SICI)1521-3935(19990101)200:1<206::AID-MACP206>3.0.CO;2-S.
(55) Kohls, D. J.; Beaucage, G. Rational Design of Reinforced Rubber. *Current Opinion in Solid State and Materials Science* **2002**, *6* (3), 183–194. https://doi.org/10.1016/S1359-0286(02)00073-6.
(56) Bauhofer, W.; Kovacs, J. Z. A Review and Analysis of Electrical Percolation in Carbon Nanotube Polymer Composites. *Composites Science and Technology* **2009**, *69* (10), 1486–1498. https://doi.org/10.1016/j.compscitech.2008.06.018.
(57) Files, B. S.; Forest, C. R. *Elastomer Filled With Single-Wall Carbon Nanotubes*; MSC-23301; 2004. https://ntrs.nasa.gov/citations/20110016657 (accessed 2024-04-20).
(58) Li, Y.; Li, M.; Pang, M.; Feng, S.; Zhang, J.; Zhang, C. Effects of Multi-Walled Carbon Nanotube Structures on the Electrical and Mechanical Properties of Silicone Rubber Filled with Multi-Walled Carbon Nanotubes. *Journal of Materials Chemistry C* **2015**, *3* (21), 5573–5579. https://doi.org/10.1039/C5TC00729A.
(59) Cruise, R. D.; Starr, S. O.; Hadler, K.; Cilliers, J. J. Triboelectric Charge Saturation on Single and Multiple Insulating Particles in Air and Vacuum. *Sci Rep* **2023**, *13* (1), 15178. https://doi.org/10.1038/s41598-023-42265-0.

(60) Talebzadeh, A.; Foudazi, A.; Kim, K.-H.; Guan, L.; Pommerenke, D. Triboelectric Charging Between Display Glass Panels and Dissipative/Insulative Rollers. *IEEE Transactions on Electromagnetic Compatibility* **2017**, *59* (6), 1755–1764. https://doi.org/10.1109/TEMC.2017.2675985.
(61) Liu, D.; Zhou, L.; Cui, S.; Gao, Y.; Li, S.; Zhao, Z.; Yi, Z.; Zou, H.; Fan, Y.; Wang, J.; Wang, Z. L. Standardized Measurement of Dielectric Materials' Intrinsic Triboelectric Charge Density through the Suppression of Air Breakdown. *Nat Commun* **2022**, *13* (1), 6019. https://doi.org/10.1038/s41467-022-33766-z.
(62) Kim, Y. J.; Lee, J.; Park, S.; Park, C.; Park, C.; Choi, H.-J. Effect of the Relative Permittivity of Oxides on the Performance of Triboelectric Nanogenerators. *RSC Adv.* **2017**, *7* (78), 49368–49373. https://doi.org/10.1039/C7RA07274K.
(63) Zou, H.; Zhang, Y.; Guo, L.; Wang, P.; He, X.; Dai, G.; Zheng, H.; Chen, C.; Wang, A. C.; Xu, C.; Wang, Z. L. Quantifying the Triboelectric Series. *Nat Commun* **2019**, *10* (1), 1427. https://doi.org/10.1038/s41467-019-09461-x.
(64) Lenhardt, J. M. *Llama 20, 40, 50 and 60 Siloxanes for Direct Ink Write – Compositional Information*; LLNL-TR-835928; Lawrence Livermore National Lab. (LLNL), Livermore, CA (United States), 2022. https://doi.org/10.2172/1871381.

TOC graphic

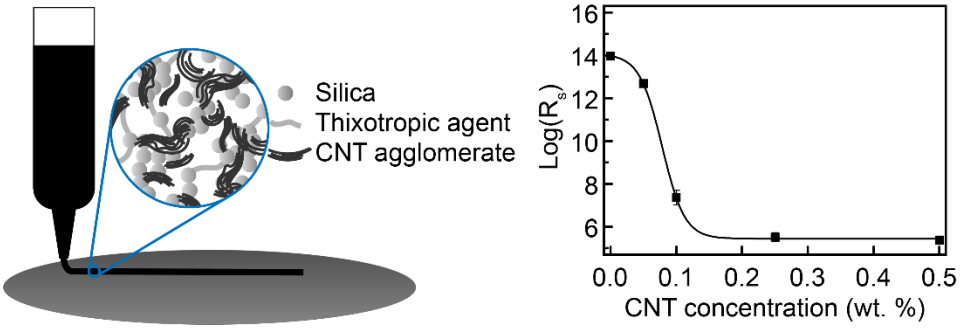

Cover Art

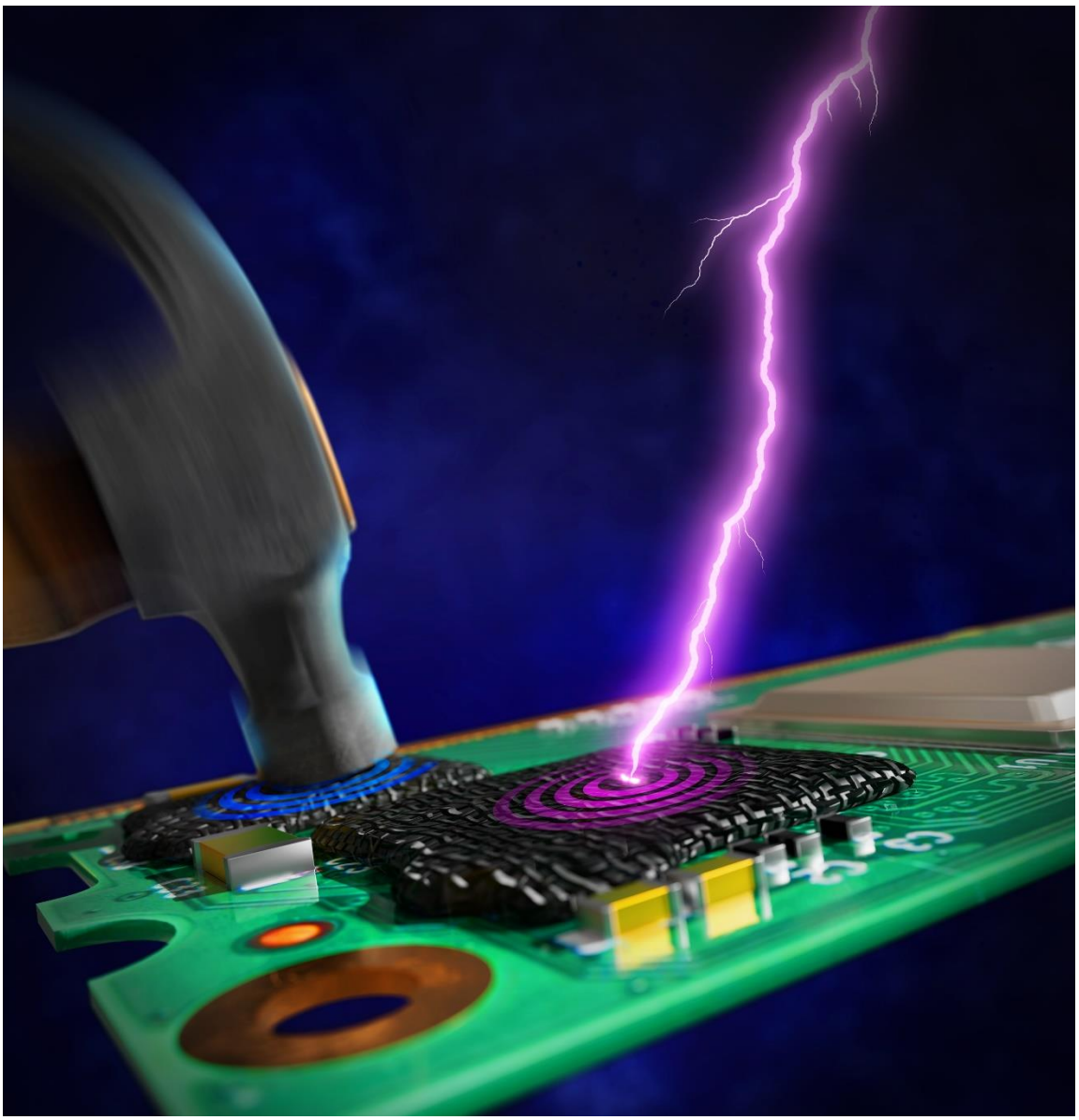

Tailored soft structures that serve as both electrostatic dissipative and mechanical shielding are developed using low loadings of single-walled carbon nanotubes (<1 wt. %) to optimize the composite for direct ink write 3D printing.